# Digital breast tomosynthesis using an amorphous selenium flat panel detector

M. Bissonnette, M. Hansroul, E. Masson, S. Savard, S. Cadieux, P. Warmoes, D. Gravel, J. Agopyan, and B. Polischuk
Anrad Corp., St-Laurent (Québec), Canada H4R 2P1

W. Haerer and T. Mertelmeier*
Siemens Medical Solutions, Erlangen, Germany

J. Y. Lo, Y. Chen, J. T. Dobbins III, J. L. Jesneck, and S. Singh
Depts of Radiology and Biomedical Engineering, Duke University Medical Center, Durham NC 27710, USA

## ABSTRACT

A prototype breast tomosynthesis system** has been developed, allowing a total angular view of ±25°. The detector used in this system is an amorphous selenium direct-conversion digital flat-panel detector suitable for digital tomosynthesis. The system is equipped with various readout sequences to allow the investigation of different tomosynthetic data acquisition modes. In this paper, we will present basic physical properties – such as MTF , NPS, and DQE – measured for the full resolution mode and a binned readout mode of the detector. From the measured projections, slices are reconstructed employing a special version of filtered backprojection algorithm. In a phantom study, we compare binned and full resolution acquisition modes with respect to image quality. Under the condition of same dose, we investigate the impact of the number of views on artifacts. Finally, we show tomosynthesis images reconstructed from first clinical data.

**Keywords:** Tomosynthesis, digital mammography, flat panel detector, selenium detector, filtered backprojection, reconstruction, DQE, MTF, NPS

## 1. INTRODUCTION

Full-field digital mammography (FFDM) offers many advantages over film/screen mammography. Although most commercial FFDM systems have shown to have superior image quality over their analog counterparts – as measured through detective quantum efficiency (DQE) – large scale clinical trials have failed to demonstrate the expected improved diagnostic efficiency[1,2]. The main reason for the diagnostic's impairment of conventional mammography (both film/screen and FFDM) is the fact that the 3-D anatomical information is projected into a 2-D image plane. Therefore, anatomical structures that overlap the tumors – and not inherent signal-to-noise ratio of the image – limit the radiologist's ability to detect certain cancers. Digital tomosynthesis for mammography has shown promise to overcome this limitation of conventional mammography by acquiring several views of the breast from different angles and reconstructing the image into a 3-D volume set.

In 1972, Grant[3] described a type of geometric tomography called tomosynthesis, which uses a conventional x-ray source and a digital detector to produce a virtually unlimited number of tomographic images at arbitrary depths in the patient. Tomosynthesis has recently enjoyed a resurgence due to several key technological developments[4] including flat-panel detectors capable of producing high-speed, high-quality digital images, as well as reconstruction and post-processing

* thomas.mertelmeier@siemens.com, phone: +49 9131 84 4707, fax: +49 9131 84 2247
** Work in progress. Not currently commercially available for sale in the U.S.

Medical Imaging 2005: Physics of Medical Imaging, edited by Michael J. Flynn,
Proceedings of SPIE Vol. 5745 (SPIE, Bellingham, WA, 2005)
1605-7422/05/$15 · doi: 10.1117/12.601622

algorithms which reduce the blur from out-of-plane structures, thereby rendering section images of much higher quality. Successful reconstruction and post-processing algorithms have included filtered backprojection and traditional shift-and-add reconstruction coupled with matrix inversion or constrained iterative restoration deblurring methods.

Breast tomosynthesis promises to improve the detection and characterization of lesions by removing overlapping dense fibroglandular tissue. The goal is to provide 3-D information at high resolution and comparable dose to mammography. Recent published work in breast tomosynthesis utilized prototypes based on commercial FFDM systems.

Niklason et al.[5] reported a modified shift-and-add tomosynthesis method, evaluated mastectomy sample images, and noted three potential benefits of tomosynthesis: (1) improve detection of lesions at screening compared to conventional mammography, particularly in dense breasts; (2) use for problem solving during diagnostic workup, since a lesion may be better observed (e.g., the lesion margins); (3) improve understanding of the 3-D relationship between a noted mass and calcifications.

Suryanarayanan et al.[6,7] evaluated various deblurring algorithms for improving breast tomosynthesis and carried out a contrast-detail study with a phantom layer sandwiched between background objects .

Wu et al.[8] evaluated tomosynthesis in both phantom and human subject data, using a maximum-likelihood expectation-maximization (MLEM) iterative reconstruction algorithm. Evaluations with mastectomy samples and human subjects were performed on a clinical tomosynthesis prototype with up to 11 projection images acquired over an angular range of 40-50°. More recently, Wu et al.[9] also presented a comparison of different reconstruction algorithms. It should be noted that this work was constrained to the acquisition configuration of 11 projections over a 50˚ angular range.

In this paper, we will present a prototype breast tomosynthesis system based on a modified full-field digital mammography device and an amorphous selenium detector suited for fast readout. The goal of this prototype tomosynthesis system is to serve as a R&D tool to gain experimental insight into the tradeoffs between acquisition speeds, reconstruction algorithms, number of views, angular span for x-ray tube, x-ray spectrum, and many other parameters which affect tomosynthesis image quality, and patient glandular dose.

## 2. METHODS AND MATERIALS

### 2.1 System and detector description

A Siemens Novation$^{DR\text{TM}}$ x-ray generator was modified to allow for an x-ray tube motion to cover an arc of $\pm 25^{o}$ relative to the pivoting point that is 6 cm above the detector surface. Hardware and software modifications were also made to the machine to allow multiple x-ray pulses to be generated during a single x-ray exposure sequence, and synchronize the x-ray pulses with the detector read/integrate cycle and x-ray tube motion. In order to get rid of mechanical instabilities as much as possible, a mode with continous tube motion was selected instead of a “step and shoot” mode which might induce vibrations. The integrated tomosynthesis system is shown in Figure 1(c) .

The detector used in this prototype tomosynthesis system is a direct converter amorphous selenium flat-panel detector. The array dimensions are 2816x3584, with a pixel pitch of 85 µm, which translates to an active area of 23.9cm x 30.5cm. The electronic gain and read time of the detector were optimized for tomosynthesis imaging. A photograph of the x-ray detector is shown in Figure 1(a) and (b).

Various image acquisition modes were designed into the system to facilitate different research objectives. From the perspective of the detector, there are essentially two modes of operation – namely full resolution and binning. In full resolution mode, the time required to read the panel is 0.6 seconds, and a programmable integration period, nominally 0.2 seconds, is used to integrate the charge on the plate. This leads to a total cycle time of 0.8 seconds, as shown in Figure 2(a). In the binning mode, a 1x2 pixel binning has been implemented inside the detector, where the binning direction is in the same direction as the tube motion during the scanning process, which also correspond to the same orientation as the data lines on the detector. In this mode, the read time for the plate has been reduced to 0.3 seconds, and a similar integration window of 0.2 seconds is also used as shown in Figure 2(b). From these two basic detector modes, several different image acquisition strategies have been defined, which vary in scan time and total number of

frames. For example, to almost completely eliminate focal spot blur, a very slow scan time of 39 seconds is used to acquire 49 different views spanning the entire $\pm 25^0$. In order to investigate the effects of image lag, modes where intermediate dark frames are acquired and combined in a recursive manner to reduce lag[10] have been implemented, as shown in Figure 2(c). Other acquisition modes which have been defined include 25 views in full resolution mode with a scan time of 20 seconds, and 25 views in binning mode with a scan time of 12.5 seconds. Table 1 summarizes the different acquisition modes implemented in the current prototype system.

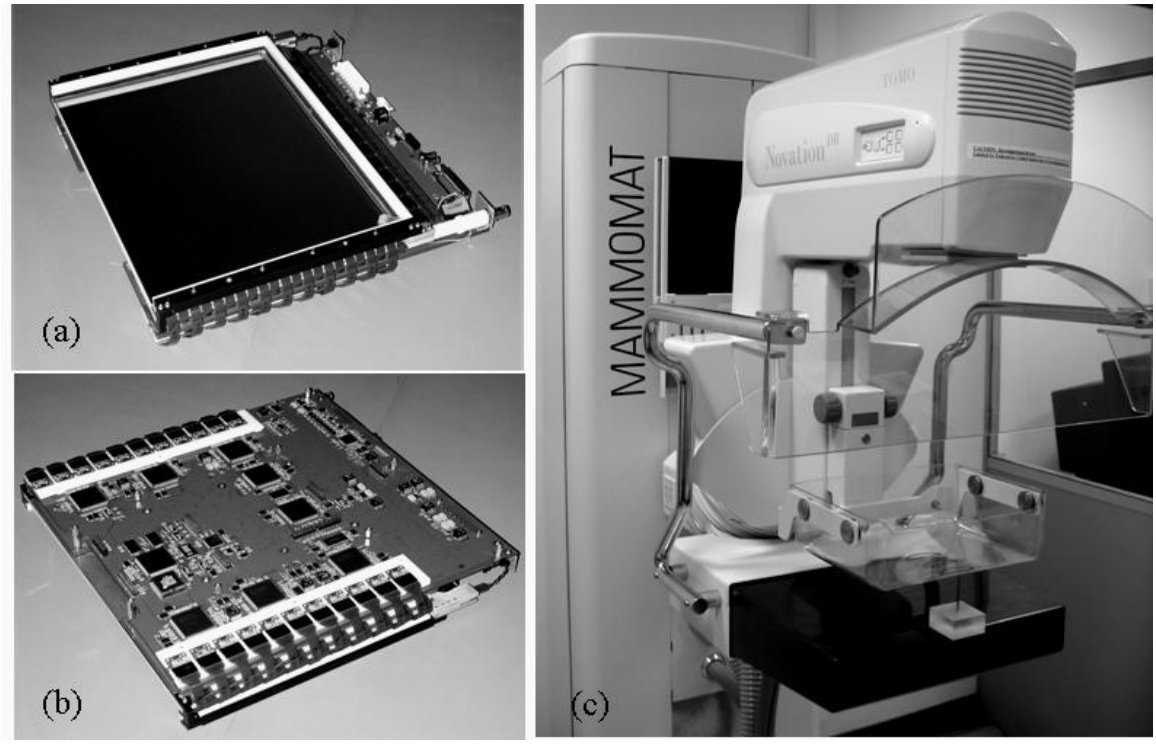


Figure 1: (a) Top view and (b) bottom view of amorphous selenium detector. (c) Photograph of prototype tomosynthesis system.

Table 1: Summary of different image acquisition modes implemented in prototype system.

| Number of views | Scan time/s | Acquisition mode | Lag correction |
|---|---|---|---|
| 49 | 39.2 | Full resolution | No |
| 25 | 40.0 | Full resolution | Yes |
| 19 | 15.2 | Full resolution | No |
| 15 | 24.0 | Full resolution | Yes |
| 11 | 17.6 | Full resolution | Yes |
| 25 | 20.0 | Full resolution | No |
| 25 | 12.5 | 1x2 binning | No |
| 25 | 25.0 | 1x2 binning | Yes |

### 2.2 Data acquisition

In this paper we report on data taken from a phantom and from human subjects. The phantom was a sponge with three inserted beans and a group of microcalcifictions taken from an ACR phantom (RMI 156). The whole sponge was put into a plastic bag filled with water. The next phase of this project was to take projection data from mastectomy specimen with the goal to set up the system with respect to dose and acquisition parameters. In this paper we will skip those images. Finally, the first clinical patient data could be acquired.

For the purpose of geometry calibration the system provides angular information for each projection. From these data, the focal position of each single view is determined under the assumption that the focal spot moves on a circular path around the pivoting point (iso-center) in the plane perpendicular to the detector and intersecting the detector plane at the chest wall side. The appropriate accuracy of this geometric model was validated imaging a plexiglass phantom with metal balls inserted.

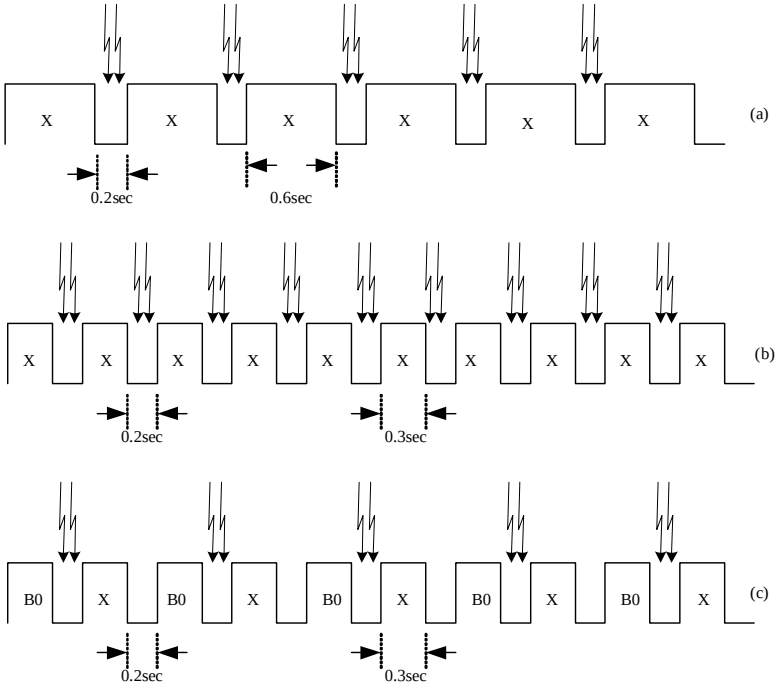


Figure 2: Various detector acquisition modes implemented in prototype tomosynthesis system. (a) Full resolution, (b) 1x2 pixel binning, and (c) 1x2 pixel binning with intermediate offset acquisition for recursive lag correction. The symbol X denotes the readout phase for the x-ray image. B0 is the symbol for the indermediate offset readout in (c).

### 2.3 Tomosynthesis image reconstruction

In this collaboration we investigate several different reconstruction methods. In this paper, however, we will focus on a reconstruction method based on filtered backprojection (FBP). The reconstruction approach described here allows a systematic filter design, an optimized image quality specific to the application, an easy adjustment of slice thickness, and strategies for reducing artifacts due to incomplete sampling of tomosynthesis.

For the image results presented here, we reformulate the reconstruction method described in ref. 11 for 2-D circular sampling in x- and y-coordinates (circular tomosynthesis). Adaptation to mammographic sampling yields - in parallel beam approximation - a linear sampling path, e.g. in y-orientation. The parallel-beam approximation is appropriate for filter design since the associated inaccuracies are small compared to the effects of inherently incomplete tomosynthetic sampling. Then it can be shown that an appropriate filter function in Fourier space can be chosen as

$$H_{filter}(\omega_y, \omega_z) = H_{spectrum}(\omega_y) \cdot H_{profile}(\omega_z) \cdot H_{inverse}(\omega_y, \omega_z), \quad (1)$$

where $H_{inverse}$ inverts the modulation transfer function $H_{projection}$ of the projection–backprojection process in the frequency region accessible by tomosynthis. For approximately equiangular sampling and small tomosynthetic (half) angle $\alpha$, $H_{projection}$ is given by

$$H_{projection}(\omega_y, \omega_z) = \frac{1}{2\alpha|\omega_y|} \quad (2)$$

For the spectral filtering $H_{spectrum}$ we chose a von Hann ('Hanning') window

$$H_{spectrum}(\omega_y) = 0.5\left(1+\cos\left(\frac{\pi\omega_y}{A}\right)\right) \tag{3}$$

with parameter A to regularize noise. In the examples shown in this paper, we omit the 'slice thickness' filter[11] $H_{profile}(\omega_z)$ completely. Thus, the filtering applied here can be characterized as a ramp filter modified by the von Hann window. In general, this method is very flexible with regard to image quality and can be adjusted to the imaging task.

For the backprojection step in FBP reconstruction it is of essence to correctly take into account the geometry of data acquisition. This is accomplished in our backprojection algorithm by employing projection matrices for each view[12,13]. The projection matrices can be determined by calibrating the system with the help of a marker phantom as described in section 2.2.

## 3. RESULTS AND DISCUSSION

### 3.1 Physical detector characterization

The physical characteristics of the detector were measured using a W/Rh x-ray spectrum filtered by 4 cm PMMA placed near the x-ray tube that was positioned at $0^o$ and not moving during the data acquisition. The x-ray beam quality and intensity were measured by suspending the ion chamber from a calibrated Keithley 3505A x-ray dosimeter 76mm above the surface of the detector. The HVL of the spectrum was evaluated to be 0.795mm Al, which according to tables published by Boone[14], yields an x-ray fluence of 57800 photons/mm$^2$/mR. Using inverse square law relationships, the actual number of photons at the selenium surface was then determined from the aforementioned fluence and measurement of the exposure value for each exposure time.

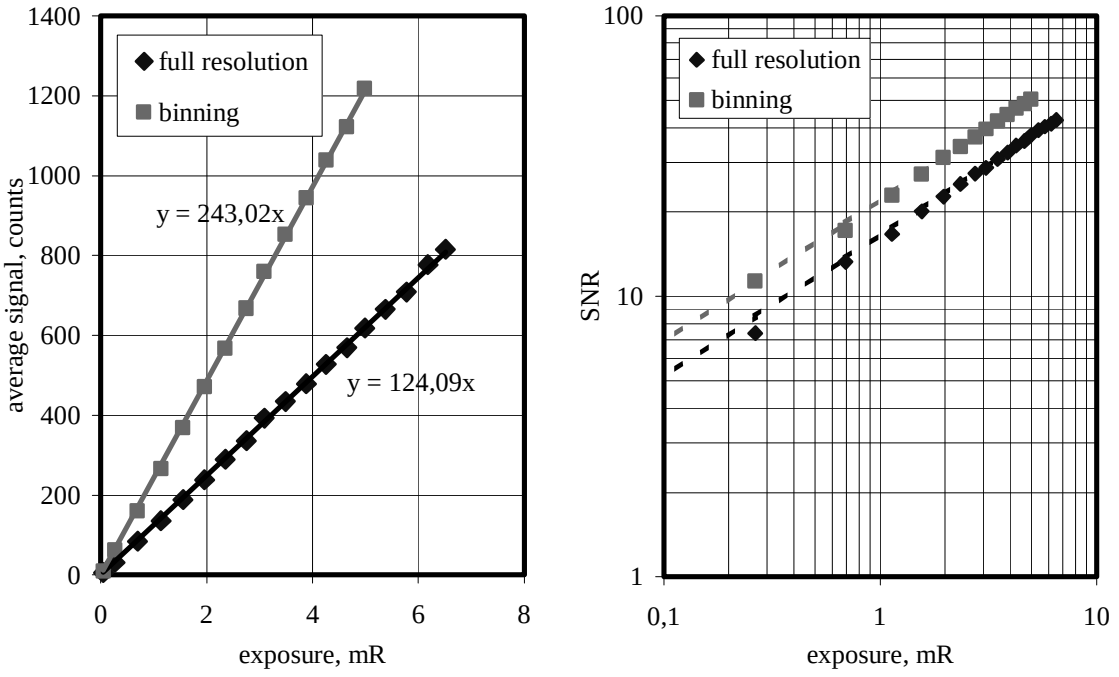


Figure 3: Plot of (a) signal conversion efficiency and (b) measured SNR as a function of detector entrance exposure for both binning and full resolution modes.

Flat-field images were acquired in both binning and non-binning modes using various exposure times to measure the characteristic response of the detector. A single frame was acquired for each exposure time, and sufficient time was allowed between each exposure to ensure that detector lag did not influence the result.

Figure 3(a) shows the characteristic curves for both binning and non-binning modes. The gain of the detector in binning mode is almost twice as large as in the full resolution mode since two pixels are read at the same time in that particular mode, and hence twice as much charge is measured by the electronics. From these flat-field measurements, the signal-to-noise properties were extracted by using a 200x200 region of interest, and the results are shown in Figure 3(b). The dotted line shows the theoretical curve one would expect if the image quality was completely quantum-noise limited. As can be seen from the measured data points in Figure 3(b), the electronic noise of the detector in both binning and full resolution modes is almost completely negligible over the exposure range investigated, which was 0.26 mR to 6.5 mR.

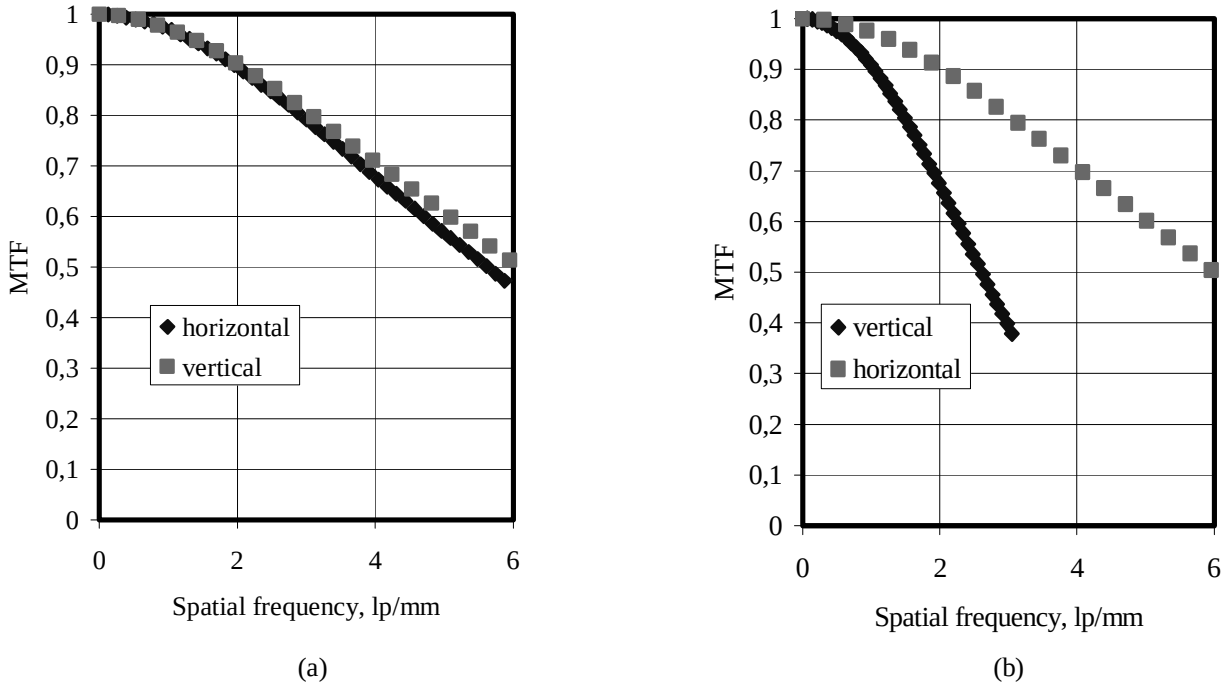


Figure 4: MTF characteristics for horizontal and vertical directions for (a) full resolution mode and (b) binning mode

The resolution of the detector was determined using a slightly angulated 10µm wide slit phantom (Nuclear Associates 07-624-1000) as described in the literature[15]. Since the resolution is anisotropic in the binning mode, the MTF was measured in both the horizontal and vertical directions. Ten images of the slit camera were acquired, and then averaged together to reduce the influence of electronic and quantum noise. Figure 4 (a) and (b) shows the resulting MTF in the full resolution mode and binning modes respectively.

The detective quantum efficiency (DQE) was then derived from the flat-field images and the measurement of the detector MTF. From each flat-field image, an ROI of 768x1024 was extracted near the location where the exposure was measured, and this ROI was subdivided into 3x4 256x256 regions. The normalized noise power spectrum (NNPS) for each sub-region was then derived by taking the square of the modulus of the Fourier transform of each sub ROI, and the resulting 12 NNSP's were then averaged together to produce the 2-D NNPS. 1-D NNPS curves were then extracted from the 2-D NNPS by taking a slice which is 16x256 for $NNPS_y$, and a slice which is 256x16 for $NNPS_x$. The resulting 1-D NNPS curves were then combined with the fluence measurements and the measurements of the corresponding MTF's to produce the resulting DQE curves, which are shown in Figure 5 for the full resolution mode, and Figure 6 for the binning mode.

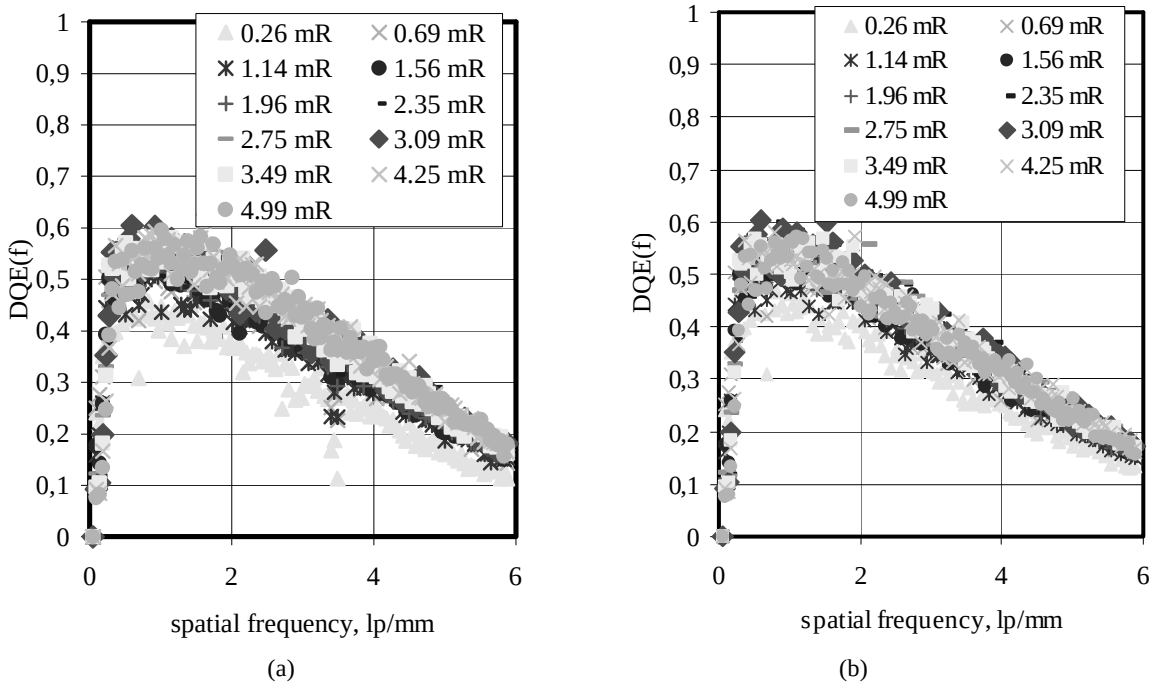


Figure 5: DQE(f) curves for various entrance exposures for full resolution mode. (a) vertical and (b) horizontal directions.

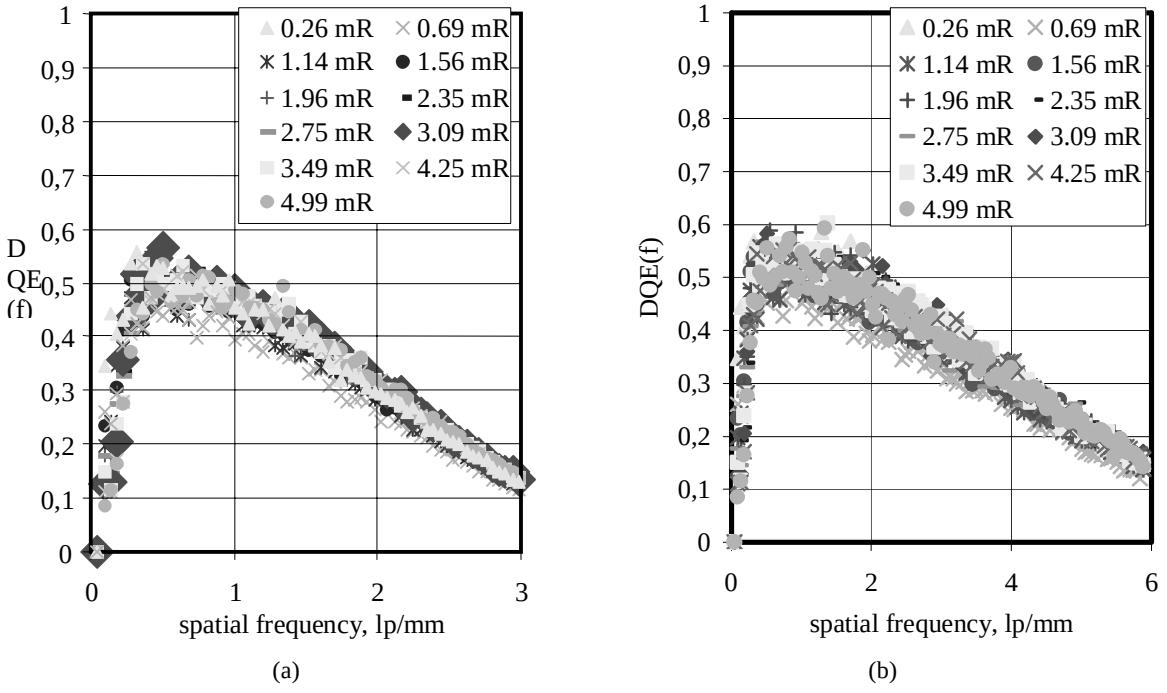


Figure 6: DQE curves for various entrance exposures for 1x2 binning mode. (a) vertical (binned) and (b) horizontal (non-binned) directions.

Despite the presence of some correlated noise in the low dose DQE measurements in the full resolution data, the relative shape and dose dependence of the DQE curves is approximately the same in both directions. This is due mainly to the essentially isotropic MTF's as a result of the square pixel aperature. By comparison, the data from the 1x2 binning mode

shows an improved dose performance in both directions, and maintains the high MTF in the non binned direction at the expense of resolution in the binned direction. Since perceived image quality is due to a tradeoff between resolution and noise, binning in an anisotropic manner as this gives the perception of improved image quality since the overall electronic noise is reduced, and only a modest reduction in resolution is noticed since it is only degraded in one direction.

### 3.2 Tomosynthesis reconstruction

#### 3.2.1 Phantom images

First, we want to investigate the influence of the data acquisition mode on image quality. The comparison between different modes is done by visual assessment of artifacts, spatial resolution, and noise. Also the reconstruction filter parameters were kept constant after some initial experiments. The parameter A for the Hanning window was chosen 0.25 for the full resolution mode with a detector pixel size of 0.085 mm. This parameter was set to 0.5 for the binned mode, both for hardware and for software binning. In all cases discussed in the following, the slice distance is 1 mm with an in-plane grid mesh for the reconstruction of 0.17 mm in both directions. Thus the voxel size for the voxel driven backprojection is 0.17mm x 0.17mm x 1 mm.

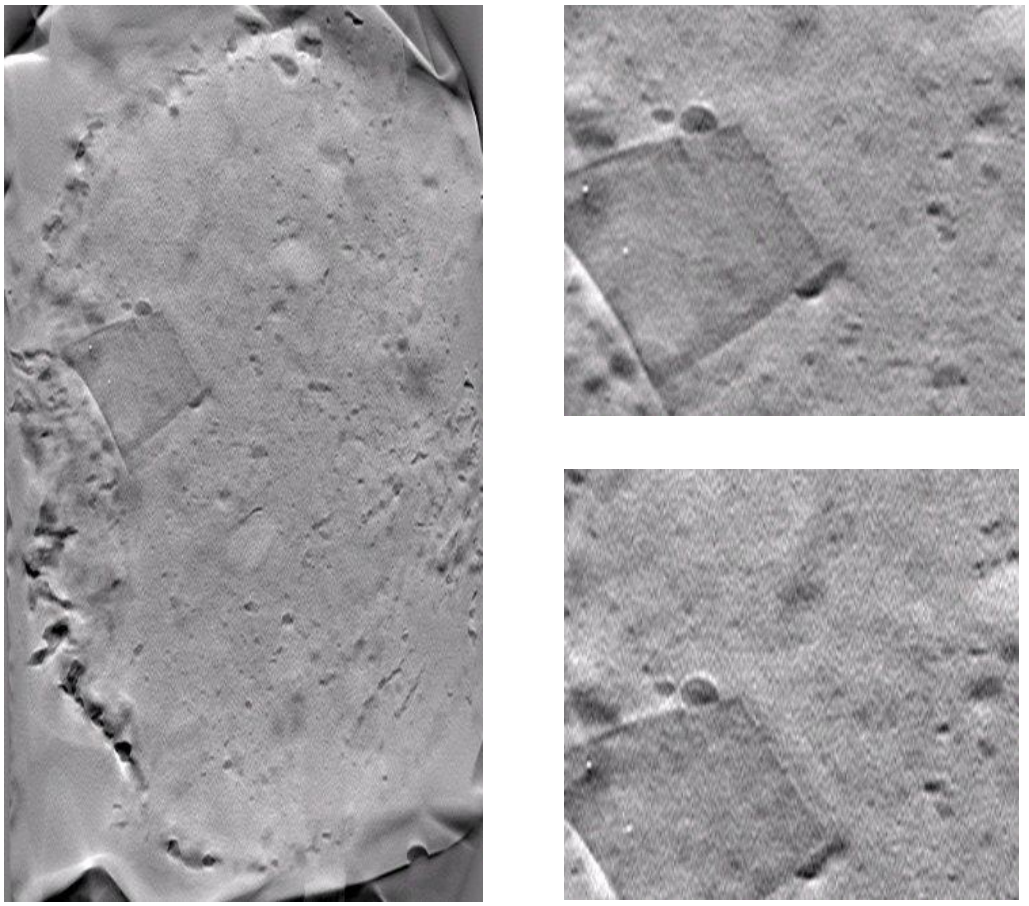

Figure 7: Reconstructed slice of the sponge phantom, (a) overview, (b) subsection containing a microcalcification structure from binned projection data, (c) from unbinned projection data.

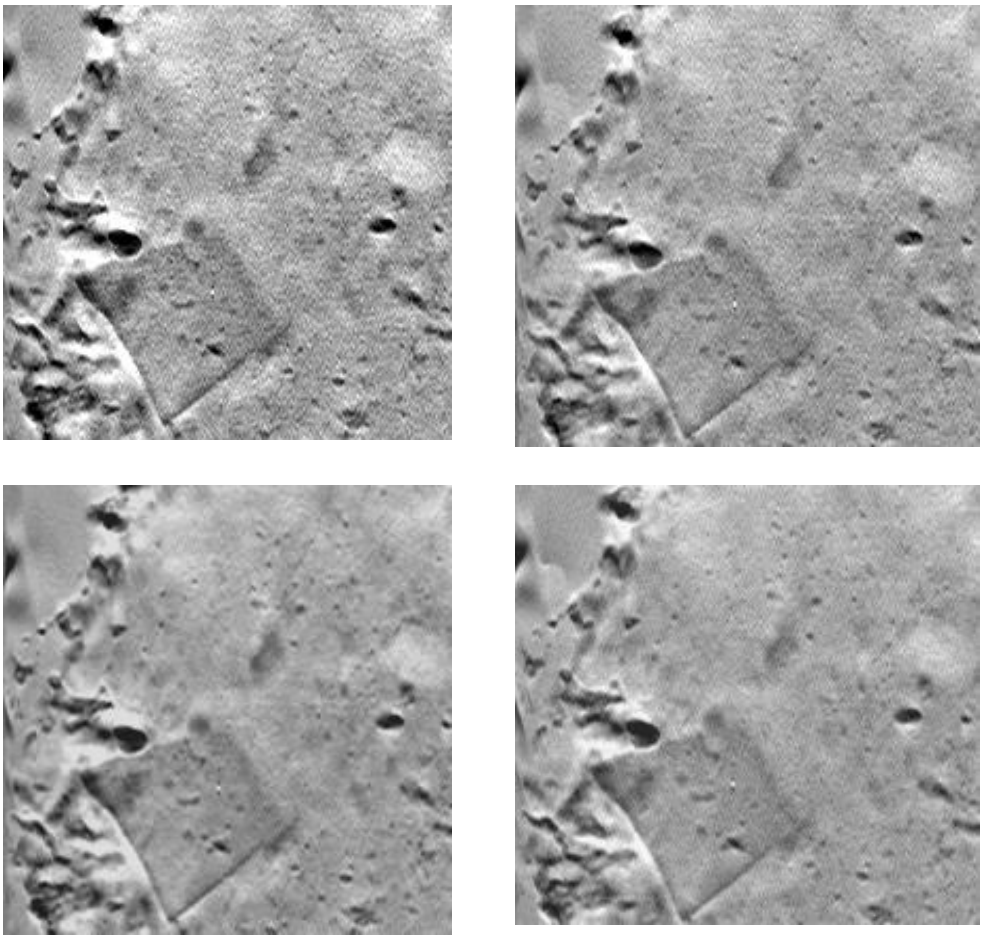

Figure 8: Reconstructed slice of the sponge phantom, (a) 13 projections (79 mAs), (b) 25 projections (79mAs), (c) 25 projections (156 mAs), and (d) 49 projections (156 mAs).

For the sponge phantom a W/Rh spectrum with 28kV and 80 mAs was chosen, which corresponds to the same x-ray technique deduced by phototiming the object on a conventional film/screen system. Figure 7 shows slice z = 24 mm (above the object support) of the sponge phantom with the microcalcification structure. In Figure 7(a) the complete slice can be seen whereas in Figure 7(b) a subsection of this slice is displayed reconstructed from the data taken in binning mode. The corresponding subsection (slightly shifted) is shown in Figure 7(c) for the unbinned projection data. The acuity of the microcalcifications appears to be the same. However, in the images reconstructed from the binned data noise seems to be reduced. In the sequel, we therefore use only binned data for reconstruction.

To study the influence of the number of views on image quality and artifacts, we performed a series of experiments with varying number of projections. In Figure 8 it is demonstrated that for 25 or more views the artifacts are largely reduced that can be seen for the case of 13 views. The data sets for Figures 8(a) and (b) and for Figures 8(c) and (d) were acquired with the same dose, respectively. Therefore, the differences and artifacts seen are solely due to the limited number of views. Note that the slice shown in Figure 8 is 3 mm above that shown in Fig. 7 and, therefore, a different microcalcification can be seen, but not the two of Figure 7.

### 3.2.2 Clinical images

Human subjects were recruited from among cases already scheduled to undergo biopsy, and informed consent was acquired in accordance with IRB approved protocols. One of the scans acquired at Duke Medical Center is shown in Figure 9. The human subject with compressed breast thickness of 6 cm underwent tomosynthesis scans on each breast in MLO position. The anode/filter combination was W/Rh with 28kVp. According to the experimental exposure tables for the FFDM system with the same tube, 133.4 mAs were applied in total for 49 projections. Figure 9 (left) displays a slice through the middle section of the compressed breast, where clearly the ducts and other fine structure are visible. Most prominent is a new invasive ductal carcinoma with some lobular component in this patient who had a biopsy 25 years ago[16]. In Figure 9 (right) a slice close to the upper surface of the breast is shown depicting the blood vessels.

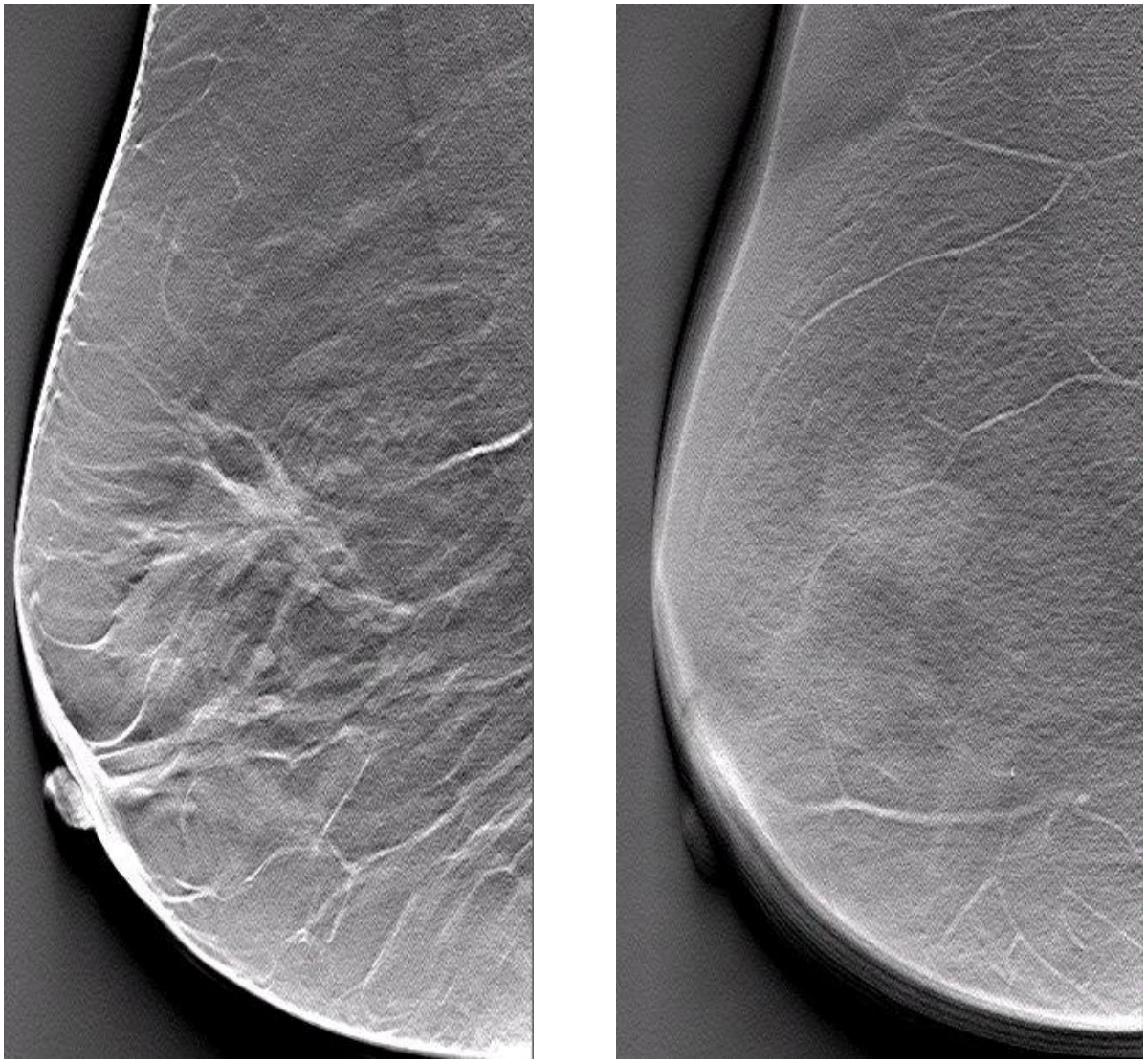

Figure 9: Reconstructed slices of a patient data set in MLO projections, (left) slice at z = 21 mm above patient table, (right) slice close to the surface of the breast[*].

[*] WIP images are works in progress and are not commercially available in the U.S.

## 4. CONCLUSION

We developed a research system for breast tomosynthesis based on an amorphous selenium direct detector with fast readout and low lag[10]. The detector is designed for high DQE to enable operation at very low exposures. This low-noise feature of the detector is particularly important if one wants to split the total exposure to many single projections for tomosynthesis reconstruction. The tungsten x-ray spectrum provided by the system helps further reducing the dose of a tomosynthesis scan.

We measured the physical image quality of the detector in binned and unbinned readout mode. The binned mode profits from improved noise performance. With phantom studies we showed that in the binned readout of the detector the frame rate could be increased to 2 frames per second, thus leading to an acceptable scan and compression time for the patient. We further demonstrated the improvement of image quality by employing more projections than previously used for breast tomosynthesis. With a number of projections of 25 and more, the streak-like limited-number-of-view artifacts can be largely reduced. First patient images promise the high potential of this breast tomosynthesis system.

For future work we plan to thoroughly study the parameters relevant for tomosynthesis data acquisition and reconstruction. Among these are the number of views required and the angular range of the scan. The detector properties such as lag and ghosting for the different readout schemes have to be investigated. Eventually, pre- and postprocessing of the data, and the image reconstruction have to be optimized.

## REFERENCES


1. Lewin JM, D'Orsi CJ, Hendrick RE, Moss LJ, Isaacs PK, Karellas A, Cutter GR, "Clinical comparison of full-field digital mammography and screen-film mammography for detection of breast cancer", Amer. J. Rad. **179**, 671-677, 2002.
2. Skaane P, Skjennald A, "Screen-film mammography versus full-field digital mammography with soft-copy reading: randomized trial in a population-based screening program – the Oslo II study", Radiology **232**, 197-204, 2004.
3. Grant DG, "Tomosynthesis: a three-dimensional radiographic imaging technique", IEEE Transactions on Biomedical Engineering **19**, 20-28, 1972.
4. Dobbins JT, III, Godfrey DJ. "Digital x-ray tomosynthesis: current state of the art and clinical potentia", Physics in Medicine and Biology **48**, R65-R106, 2003.
5. Niklason LT, Christian BT, Niklason LE, et al., "Digital tomosynthesis in breast imaging", Radiology **205**, 399-406, 1997.
6. Suryanarayanan S, Karellas A, Vedantham S, et al., "Comparison of tomosynthesis methods used with digital mammography", Academic Radiology **7**, 1085-1097, 2000.
7. Suryanarayanan S, Karellas A, Vedantham S, et al., "Evaluation of linear and nonlinear tomosynthetic reconstruction methods in digital mammography", Academic Radiology **8**, 219-224, 2001.
8. Wu T, Stewart A, Stanton M, et al., "Tomographic mammography using a limited number of low-dose cone-beam projection images", Medical Physics **30**, 365-380, 2003.
9. Wu T, Moore R, Rafferty EA, Kopans DB, "A comparison of reconstruction algorithms for breast tomosynthesis", Medical Physics **31**, 2636-2647, 2004.
10. Loustauneau V., Bissonnette M., Cadieux S., Hansroul M., Masson E., Savard S., and Polischuk B., "Ghosting comparison for large-area selenium detectors suitable for mammography and general radiography", Proc. SPIE **5368**, 162-169, 2004.
11. Lauritsch G, Haerer WH, "A theoretical framework for filteres backprojection in tomosynthesis", Proc. SPIE, **3338**, 1127-1137, 1998.
12. Wiesent K, Barth K, Navab N, Durlak P, Brunner TM, Schuetz O, Seissler W, "Enhanced 3-D reconstruction algorithm for C-arm systems suitable for interventional procedures", IEEE Transactions on Medical Imaging, vol. **19**(5), 391-403, 2000.
13. Strobel NK, Heigl B, Brunner TM, Schuetz O, Mitschke MM, Wiesent K, Mertelmeier T, "Improving 3D image quality of X-ray C-arm imaging systems by using properly designed pose determination systems for calibrating the projection geometry." Proc. SPIE **5030**, 943-954, 2003.

14. Boone J, “Spectral modeling and compilation of quantum fluence in radiography and mammography”, Proc. SPIE **3336**, 592-601, 1998.
15. Fujita H, Tsai DY, Itoh T, Doi K, Morishita J, Ueda K, and Ohtsuka A, “A simple method for determining the modulation transfer function in digital radiography”, IEEE Transactions on Medical Imaging, vol. **11**(2), 34-39, 1992.
16. J. Baker, Duke University Medical Center, private communication, 2005.